Magnetic structure factor in cuprate superconductors: Evidence for charged meron vortices

Mona Berciu[1] and Sajeev John[2]
[1]*Department of Physics and Astronomy, University of British Columbia, Vancouver, British Columbia V6T 1Z1, Canada*
[2]*Department of Physics, University of Toronto, 60 St. George Street, Toronto, Ontario, M5S 1A7, Canada*
(Received 2 February 2004; published 30 June 2004)

In this paper we demonstrate that a ground state consisting of a quantum liquid of merons and antimerons can quantitatively describe the position and orientation of the incommensurate peaks observed in elastic neutron scattering on cuprates, with essentially no free or adjustable parameters. At small dopings, the relevant length scale is the transverse size of a meron-antimeron pair, defined by the doping concentration. This results in a displacement of the incommensurate peaks from (π,π) which is proportional to doping. At higher dopings, the meron core size becomes relevant, leading to a saturation of the displacement. The formation of stripe-like phases at $\delta=1/8$ and the suppression of the superconductivity is also recaptured in this model.

DOI: 10.1103/PhysRevB.69.224515 PACS number(s): 74.20.Mn, 71.27.+a, 71.10.Fd

I. INTRODUCTION

Magnetism is central to the phenomenology of the high-temperature superconducting cuprates. Neutron scattering experiments directly probe the arrangement of electronic moments $\{\vec{S}_n\}$. In particular, the magnetic neutron elastic scattering cross section is[1]

$$\frac{d\sigma}{d\omega} \sim |\vec{F}_m(\vec{q})|^2 - \frac{|\vec{q}\cdot\vec{F}_m(\vec{q})|^2}{q^2}, \tag{1}$$

where

$$\vec{F}_m(\vec{q}) = \frac{1}{\sqrt{N}}\sum_n e^{i\vec{q}\cdot\vec{r}_n}\vec{S}_n \tag{2}$$

is the magnetic structure factor. The positions of elastic neutron scattering peaks allow identification of the magnetic structure, while their intensity is related to the local staggered magnetization.

The cuprate undoped parent compounds exhibit long-range antiferromagnetic order (LR AFM) order, with the main magnetic Bragg peak at $\vec{Q}=(\pi/a,\pi/a)$, where a is the lattice constant.[2,3] While very low doping $\delta\simeq 0.02$ destroys the long-range AFM order, robust short-range AFM correlations are observed well into the superconducting phase.[4] For $\delta>0.02$, the magnetic Bragg peak splits into four incommensurate peaks symmetrically placed about $\vec{Q}$. Their distance from $\vec{Q}$ increases linearly with doping up to around $\delta=0.12$, above which it saturates.[5–7] For $\delta\leqslant 0.05$, the four peaks are arranged diagonally in the Brillouin zone, while for $0.05<\delta<0.12$ they are centered along the vertical and horizontal (colinear) directions at[5]

$$\vec{q}_\delta = \frac{\pi}{a}(1,1\pm 2\delta) \text{ and } \vec{q}_\delta = \frac{\pi}{a}(1\pm 2\delta,1). \tag{3}$$

These peaks have been observed initially in LaCuO, but more recently also in YBaCuO.[8,9] They appear to be a generic feature of the cuprates.

An early interpretation of these incommensurate peaks, based on the assumption of a large nested Fermi surface,[10] was contradicted by angle resolved photoemission spectroscopy (ARPES) measurements which reveal no large Fermi surface in the underdoped state.[11–13] Another interpretation is linked to the generation of various spiral spin-density waves states,[14] whose pitch varies linearly with the doping concentration. A third proposal is based on the existence of charged stripes in the AFM background,[15–17] while a fourth proposal is based on the QED_3 model of the pseudogap phase.[18] In this paper we demonstrate that a ground state consisting of a quantum liquid of merons and antimerons can quantitatively describe the position and orientation of the incommensurate peaks observed in elastic neutron scattering on cuprates, with essentially no free or adjustable parameters.

Merons (antimerons) are vortices in the spin configuration with winding number $+1(-1)$, which trap a doping hole in their core (see Fig. 1). They are nucleated upon doping a modified version of the Hubbard model,[19–21] in which the

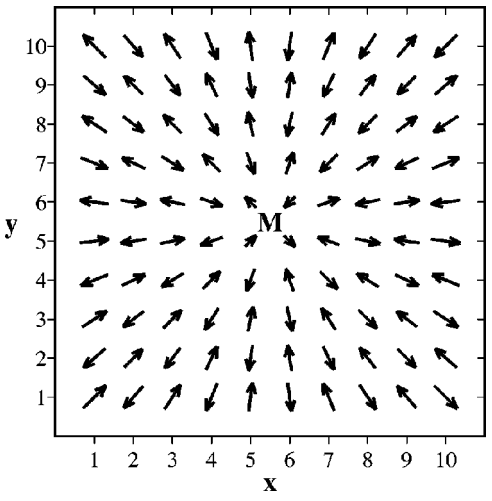

FIG. 1. Spin distribution $\vec{S}_n$ for an isolated meron vortex on a 10×10 lattice. The meron is centered on the plaquette marked by M. The spins of either magnetic sublattice rotate by 2π on any closed path that surrounds the vortex core. This self-consistent configuration was obtained within the static Hartree-Fock approximation for the spin-flux Hamiltonian (see Ref. 19).

effective one-electron dispersion relations at half filling match those measured with ARPES.[11] In other words, there are four Fermi points at $\vec{k}=\pi/2a(\pm 1,\pm 1)$ with isotropic dispersion in their vicinity. The isotropic dispersion near the Fermi points favors the appearance of textures with azimuthal symmetry, i.e., vortices or merons, upon doping. This is in sharp contrast to the conventional Hubbard and *t-J* models, which predict large nested Fermi surfaces near half filling (not observed experimentally). The highly anisotropic dispersion near such an extended Fermi surface favors the appearance of quasi one-dimensional (1D) textures with doping, i.e., charged stripes.[15–17] This assertion is supported by numerical studies[22] which show that the addition of a small second-nearest neighbor hopping to the Hubbard or *t-J* model, which decreases this anisotropy by increasing the dispersion along the $(0,\pi/a)-(\pi/a,0)$ direction, also suppresses the stripe formation.

We have shown that the merons are *mobile charged bosons*,[19–21] since the magnetic vortex carries a total spin zero and traps exactly one hole. This bosonic nature of the charge carriers provides a natural and compelling mechanism for the non-Fermi metal observed above the superconducting phase. Furthermore, given their topological nature, merons and antimerons can only be nucleated in pairs, such that the total topological (winding) number remains zero. In a semiclassical picture, there is a strong logarithmic attraction between each meron and antimeron, since the further away a meron is moved from an antimeron, the more spins in between them are rotated out of their AFM background orientation, and the more magnetic exchange energy is lost. This strong attractive force, which at intermediate range overcomes the Coulomb repulsion between the charged cores, provides a very natural charge pairing mechanism within a purely repulsive two-dimensional (2D) electron system. We have recently demonstrated that the wave function describing stable meron-antimeron pairs has *d*-wave rotational symmetry.[20] As a result, the charged bosonic meron-antimeron pair acts as a preformed "Cooper pair" of the *d*-wave superconducting state. This microscopic model provides a plausible answer to the two most puzzling questions of the high-temperature superconductivity physics, namely (1) what is the nature of the nonquasiparticle-like charge carriers responsible for the non-Fermi liquid metal observed above the superconducting state, and (2) how can strong pairing occur in a purely repulsive electron system. This microscopic model also provides a unified description (with no free or adjustable parameters) for the observed midinfrared optical absorption, destruction of long-range AFM order with doping and aspects of ARPES.[19–21]

It was independently suggested[23,24] that this modified Hubbard model, called the spin-flux model, can be derived from a fundamental, previously unrecognized, kinematic property of spin-1/2 electrons as they execute a closed trajectory in coordinate space. This concept is entailed in the proposition that a type of many-electron wave function underlies the observed antiferromagnetic spin liquid. In this quantum state, electrons undergo a 2π rotation (somersault) in their internal space of Euler angles as they traverse an elementary closed loop (plaquette) of the two-dimensional (2D) lattice. This lowers the many-body energy relative to that of a conventional AFM and has the immediate consequence that at half filling, the effective one-electron dispersion relations quantitatively agree with the ARPES data[20,21] without the need for ad hoc band structure parameters.[12] The incorporation of the correct one-electron dispersion from the outset then reveals that doping leads to the nucleation of merons and antimerons.

The paper is organized as follows: in Sec. II, we consider the 1D analog of charged merons, the charged domain walls.[25–27] The simpler 1D case provides valuable intuition on the effect of topological excitations on the magnetic structure factor. In Sec. III we demonstrate that a liquid of merons and antimerons has a magnetic structure factor which is in quantitative agreement with experiments. We do this using a very simple model to simulate the spin distributions of such a liquid of merons and antimerons. The only parameters are the doping δ, which defines the concentration of vortices, and the vortex core size ρ, which characterizes the localization length of a hole in the vortex core. In Sec. IV we briefly analyze the 1/8-doping case, and show that it too can arise from having merons and antimerons organized in a specific way, in agreement with the Tranquada configuration.[28] Section V contains the conclusions.

II. ILLUSTRATIVE EXAMPLE: DOMAIN WALLS ON A 1D AFM CHAIN

Consider a chain of lattice constant *a* parallel to the *x* axis and let $\vec{S}_n=S_n\vec{e}_y$ be the expectation value of the spin at site *n*, where $\vec{e}_y$ is a unit vector parallel to the *y* axis. For a hypothetical chain with LR AFM characterized by $S_n=(-1)^n S$, elastic neutron scattering would detect the structure factor

$$F_m(q)\sim\delta_{q,Q}, \tag{4}$$

where $Q=\pi/a$ is the 1D AFM wave vector.

In previous work based on the Hartree-Fock and configuration interaction methods,[25–27] we demonstrated that essential features of the exact Bethe ansatz solution of the 1D Hubbard chain can be recaptured by considering fluctuations around a hypothetical AFM mean field, in which each hole added to AFM Hubbard chain nucleates a magnetic domain wall. The magnetic domain wall mediates a transition from one mean-field AFM ground state ("1") to the degenerate mean-field AFM ground state ("2") in which all spins are flipped (i.e., $S\rightarrow -S$). The essential fluctuation (tunneling) correction to mean-field theory is the quantum mechanical, translational motion of the charged domain wall along the length of the chain. The resulting spinless charged domain wall is a bosonic collective excitation with high mobility and dispersion in excellent agreement with the Bethe ansatz.[27]

The appearance of a single domain wall has a drastic effect on the magnetic structure factor at $q=Q$, as shown in Fig. 2. Mathematically, the spin distribution in the presence of a domain wall is well described by[26]

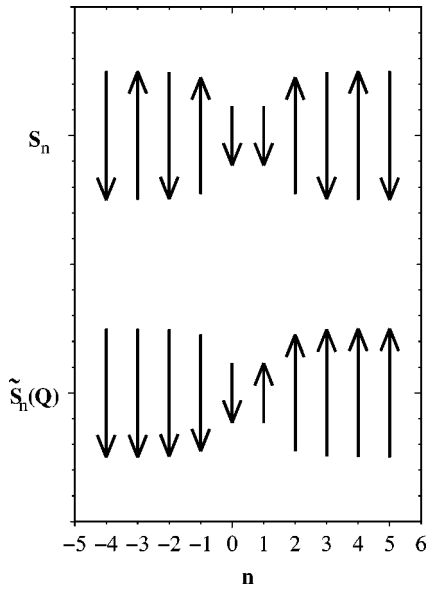

FIG. 2. Spin distribution S_n for a chain with a domain wall centered at $x_o=0.5$ and with a domain-wall radius $\rho=1$ (upper panel). For convenience, $\tilde{S}_n(Q)=\exp(iQna)S_n$ is shown in the lower panel. By symmetry, $F_m(Q)=\Sigma_n\tilde{S}_n(Q)=0$.

$$S_n=(-1)^n S\tanh\left(\frac{n-x_o}{\rho}\right), \tag{5}$$

where S is the staggered magnitude of the spins, x_o is the position of the domain wall ($x_o=0.5$ in Fig. 2) and ρ is the domain-wall radius measured in units of a. Physically, ρ characterizes the localization length of the hole trapped in the core of the domain wall. In the 1D Hubbard model, $\rho\sim t/U$, where t is the nearest neighbor hopping and U is the on-site Coulomb repulsion.[26,27] Since the hyperbolic tangent is an odd function, it follows that in the presence of even one domain wall with arbitrary ρ, the cross section for magnetic scattering vanishes at the AFM wave-vector Q, where it is maximum in the undoped case.

Clearly, a chain with cyclic boundary conditions can only accommodate an even number of domain walls, with each domain wall (associated with a π flip of the AFM order from ground-state "1" to ground-state "2") followed by an antidomain wall (associated with the π-flip of the AFM order back from ground-state 2 to ground-state 1). $F_m(Q)$ still vanishes for any $\delta\neq 0$, since on average the distribution $\tilde{S}_n(Q)=\exp(iQna)S_n$ contains as many spins up as down. However, for finite dopings a new length scale appears, defined by the average distance d between domain walls. Since each hole is trapped in the core of one domain wall, $d=a/\delta$, where δ is the doping concentration. As a result, the magnetic structure factor becomes nonzero at the incommensurate wave vectors

$$q_d^{(\pm)}=Q\pm\frac{\pi}{d}=\frac{\pi}{a}(1\pm\delta). \tag{6}$$

A pictorial demonstration for this is provided in Figs. 3 and 4. In Fig. 3 we plot the spin distribution S_n for a cyclic chain of 32 sites with four domain walls (upper panel). In the middle panel we plot $\tilde{S}_n(Q)$, and by symmetry it is apparent that $F_m(Q)=\Sigma_n\tilde{S}_n(Q)=0$. This equality also holds if the distances between the domain walls fluctuate randomly, since on average there are still equal numbers of up and down $\tilde{S}_n(Q)$ values. The lower panel shows the real part of $\tilde{S}_n(q_d^{(\pm)})=\exp(iq_d^{(\pm)}na)S_n$. While the $\exp(iQna)$ phase factor eliminates the fast (AFM) oscillations, the $\exp[i(q_d^{(\pm)}-Q)na]=\exp(\pm i\pi na/d)$ phase factor eliminates the slower domain-wall alternation.

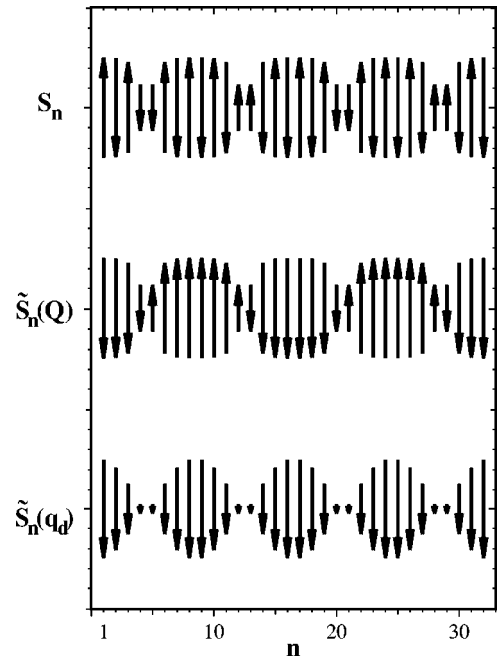

FIG. 3. Spin distribution S_n for a cyclic chain with 32 sites and four domain walls with $\rho=1$ centered at $x_o=4.5$, 12.5, 20.5, and 28.5 (upper panel). $\tilde{S}_n(Q)=\exp(iQna)S_n$ is shown in the middle panel. By symmetry, $F_m(Q)=\Sigma_n\tilde{S}_n(Q)=0$. In the lower panel we show $\mathrm{Re}\tilde{S}_n(q_d)=\mathrm{Re}[\exp(iq_dna)S_n]$. Clearly, $F_m(q_d)=\Sigma_n\tilde{S}_n(q_d)\neq 0$.

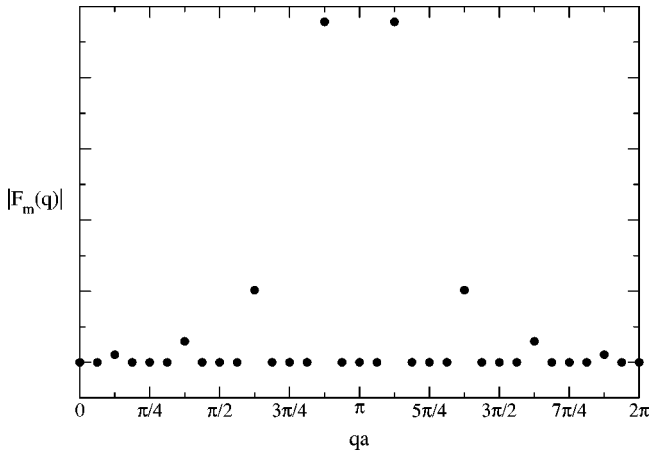

FIG. 4. Absolute value of the magnetic structure factor for the chain shown in Fig. 3, as a function of qa. $|F_m(q)|$ has two main peaks at $q_d=Q\pm\pi/d$, where $d=8a$ is the average distance between consecutive domain walls. Smaller satellite peaks at higher order harmonics are also visible.

The absolute value of the magnetic structure factor $F_m(q)$ for this 32-site chain is shown in Fig. 4. The cyclic chain has $N=32$ sites, therefore only the discrete wave vectors $q=2\pi/Nam$, with $m=0,\ldots,N-1$ (the first Brillouin zone) are considered. Instead of a single large peak at $Q=\pi/a$, characteristic of the LR AFM undoped chain, there are two satellite peaks at $q_d^{(\pm)}$. Some higher harmonics are also present. The positions of these satellite peaks shift away from Q as the doping increases. Fluctuations of the distance between successive domain walls lead to a finite width of these satellite peaks.

The difference between the hypothetical undoped chain described above and a purely one-dimensional chain in its ground state is related to the presence of charge-neutral domain wall solitons.[27] These neutral domain walls are responsible for the destruction of the LR AFM order for the undoped chain (as predicted by the Mermin-Wagner theorem). The concentration of neutral domain walls is of the order $1/\xi$, where ξ is the AFM correlation length in the undoped state. If the doping holes become bound to these preexisting domain walls, the initial peak structure in magnetic neutron scattering data will be independent of doping. Only if the doping is large enough that extra domain walls must be created over and above the pre-existing ones, will the peak positions shift substantially with doping concentration. Such behavior has been observed[29] in the quasi-one-dimensional ($S=1$) oxide, $Y_{2-x}Ca_xBaNiO_5$, whose undoped ($x=0$) parent is a quantum spin liquid. Here, doping is accompanied by incommensurate peaks whose position is initially independent of the doping concentration.

Our hypothetical AFM chain is a useful model for a one-dimensional compound embedded in a three-dimensional crystal structure. Here, small interactions with the host crystal stabilize the LR AFM order below a characteristic temperature determined by crystal field interactions. In this case, there are no neutral domain walls in the undoped state at zero temperature. As a result, the shift of the double-peak structure increases linearly with doping, as described above. However, for large dopings, the domain-wall core size ρ increases as domain-wall cores start to overlap, and eventually becomes comparable to the average spacing between domain walls. As this second length-scale becomes relevant, the incommensurate peaks are no longer expected to exhibit a simple linear shift with further doping.

III. TWO-DIMENSIONAL AFM PLANES

In direct analogy with the 1D chain described above, an undoped AFM on a 2D square lattice of lattice constant a (with long-range order imposed by weak interactions with a 3D host crystal) exhibits a magnetic neutron scattering peak at the AFM wave-vector $\vec{Q}=\pi/a(1,1)$

$$|\vec{F}_m(\vec{q})| \sim \delta_{\vec{q},\vec{Q}}. \tag{7}$$

This Bragg magnetic peak is a characteristic of undoped cuprate parent compounds.[2,3]

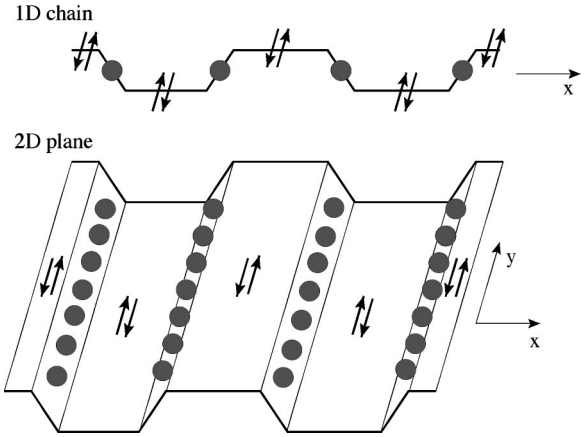

FIG. 5. Schematic representation of a 1D chain with several charged domain walls. Each domain wall mediates the transition from one AFM ground state to the other one and has a hole trapped in its core. A 2D plane with parallel stripes can be thought of as being obtained from the corresponding 1D chain through translation along the stripe backbones. The doping holes are trapped in the stripe backbone.

A. Charged vortex stripes

The appearance of the incommensurate peaks in the magnetic structure factor has been proposed as evidence for charged stripes.[15–17] A stripe is a topological line defect (domain wall) mediating a π flip from one AFM ground state to the other one ($S\rightarrow -S$), with the doping holes trapped along the stripe backbone (see Fig. 5). Following our analysis of the 1D domain walls, it is apparent that stripes suppress the magnetic structure factor at the AFM wave-vector $\vec{Q}$, i.e., $F_m(\vec{Q})\rightarrow 0$. However, if the average distance between the stripes is d, then two satellite incommensurate peaks will appear in the magnetic structure factor at the wave-vectors

$$\vec{q}_{x,d}=\left(\frac{\pi}{a}\pm\frac{\pi}{d},\frac{\pi}{a}\right). \tag{8}$$

From Eqs. (8) and (3), the peaks of the stripe model are found to match the experimental peaks if

$$\frac{d}{a}=\frac{1}{2\delta} \tag{9}$$

The factor of 2 appearing in Eq. (9) indicates that the stripes must be half filled with holes, i.e., that only every second site along the stripe backbone traps a hole. In order to explain the observed four satellite peaks of the magnetic structure factor, it is also necessary that half of the CuO planes contain stripes oriented in the x direction while the remaining CuO planes contain stripes oriented in the y direction. The rotation of the peaks from the horizontals to the diagonals below $\delta=0.05$ would likewise require a 45° rotation of all the stripes to opposing diagonal orientations on alternating CuO planes. Finally, inelastic neutron scattering data is associated with dynamical fluctuations of the stripe structures.

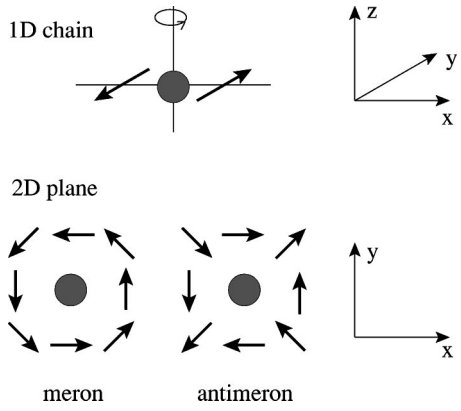

FIG. 6. Schematic representation of the 1D charged domain wall. For simplicity, we only show the orientation of the spins on one magnetic sublattice (the spins on the other sublattice are locally antiparallel). If we perform a $\pm 2\pi$ rotation of this structure about an axis centered in its core, we obtain a 2D spin vortex or antivortex, with the doping hole trapped in the vortex core. We call such objects merons or antimerons.

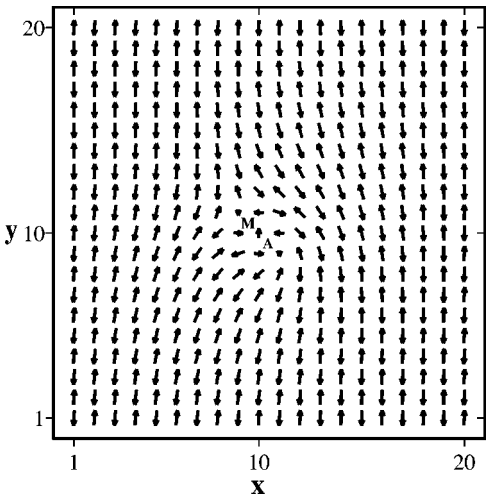

FIG. 7. Spin distribution for a tightly bound meron-antimeron pair. The meron (M) and the antimeron (A) are localized on neighboring plaquettes. The total winding number of the pair is zero. The magnetic AFM order is disturbed only in the neighborhood of the vortices. This self-consistent configuration was obtained within the static Hartree-Fock approximation for the spin-flux Hamiltonian (see Ref. 19).

Although stripes can be obtained in mean-field approximations of the doped Hubbard model,[15–17,19] the self-consistent solutions require one hole per backbone site. As such, they describe insulators, in contradiction to experiments. More recently, stripes with different (not necessarily one-half) filling factors have been found in the *t-J* model[30] using a density matrix renormalization group approach, and also in the Hubbard model,[31] using dynamical mean-field theory methods. However, other numerical calculations show conflicting results.[32] Stripes have been proposed, in a more heuristic sense, as a balance between the energy gain of charge carriers which phase separate from AFM insulating regions and the energy cost of electrostatic Coulomb repulsion among the holes.[33] Given these difficulties and the detailed tuning needed to reconcile the stripe model with the observations, it is interesting to explore a simpler and more natural explanation of the neutron scattering experiments.

B. Merons and antimerons

A simple explanation of the detailed aspects of magnetic neutron scattering is related to the nucleation of mobile $2\pi(-2\pi)$ spin vortices (antivortices) which trap the charge carriers in their vortex cores, i.e., merons and antimerons.[19,20,25,26] They represent the second natural generalization of the 1D charged domain wall to a topological excitation of the 2D plane. As shown schematically in Fig. 6, along any line that passes through the core of the meron, the magnetic order is that of a 1D domain wall. Whereas the charged stripes are line defects (see Fig. 5), the merons are point-like excitations.

The spin distribution $\vec{S}_n$ for one isolated meron vortex is shown in Fig. 1. The spins of either magnetic sublattice rotate by 2π along any closed path surrounding the vortex core. For symmetry reasons, it is again apparent that $\vec{F}_m(\vec{Q})=\Sigma_n \vec{S}_n \exp(i\vec{Q}\cdot\vec{r}_n)=0$. This means that the spins belonging to the vortex have a vanishingly small contribution to the magnetic structure factor at precisely the antiferromagnetic wave vector $\vec{Q}$.

In the case of very low doping, there are very few merons and antimerons nucleated by the doping holes. Each meron is tightly bound to an antimeron, and the various meron-antimeron pairs are separated by large regions of spins in the AFM background. Such an isolated tightly bound meron-antimeron pair is shown in Fig. 7. The magnetic structure factor of such a configuration still has a single large peak at the AFM wave vector $\vec{Q}$, since all the spins in the AFM background are contributing to it. As discussed, the spins belonging to the meron-antimeron pair have vanishing contribution to $\vec{F}_m(\vec{Q})$, and thus the intensity of the Bragg peak decreases as the density of meron-antimeron pairs (i.e., the doping concentration) increases. However, as long as various meron-antimeron pairs are well separated, the system exhibits long-range AFM order.

Self-consistent Hartree-Fock calculations (carried out on a model $U/t=5-7$) reveal that tightly bound meron-antimeron pairs distort the spin orientation of about 100 sites (see Fig. 7). Consequently, for dopings $\delta>0.02$ the meron-antimeron pairs start to overlap and each spin of the lattice is engulfed by either a meron or an antimeron vortex. Since the contribution of each vortex to $F_m(\vec{Q})$ is vanishingly small and there are no unaffected AFM background spins remaining, it follows that above $\delta\sim 0.02$ the magnetic neutron scattering intensity at $\vec{Q}$ is suppressed. This provides a simple and natural explanation for the experimentally observed suppression of the long-range AFM order at $\delta\sim 0.02$.

For $\delta>0.02$, different meron-antimeron pairs are in direct contact with one another. The magnetic interactions between vortices depend logarithmically on the inter-vortex distance r

$$E(r) \sim -J\nu_1\nu_2 \ln \frac{r}{\rho}, \tag{10}$$

where $J=4t^2/U$ is the exchange integral, and ν_1, ν_2 are the corresponding topological numbers ($\nu=1$ for a meron, $\nu=-1$ for an antimeron). Since the merons and antimerons are charged, there is a hard core repulsion between them in addition to this logarithmic interaction. Minimization of this total energy suggests a crystal-like ground state, with alternating merons and antimerons frozen on an ordered superlattice. However, each meron-antimeron pair can significantly lower its energy through translational and rotational motion. The kinetic energy thus gained is of the order of t for each vortex[20] and more than compensates the loss of exchange energy ($J \sim t^2/U < t$) caused by "melting" the meron crystal configuration. As a result, we expect the ground state to be a two-component quantum liquid, with the charged merons and antimerons dynamically moving over the entire lattice.

In order to estimate its magnetic structure factor, we consider a simplified model of this ground state: we average over many random distributions of merons and antimerons, corresponding to different "snapshots" of the quantum liquid. Such snapshots are simulated as follows. We randomly choose the positions $\vec{R}_{M,i}$ and $\vec{R}_{A,i}$, with $i=1, N_0$, of the centers of the N_0 merons and antimerons on a $N \times N$ lattice, corresponding to a nominal doping $\delta=2N_0/N^2$. For any site $\vec{r}=x\vec{e}_x+y\vec{e}_y$ of the lattice, we define

$$\phi(\vec{r}) = \sum_{i=1}^{N_0} \left(\tan^{-1} \frac{y - Y_{M,i}}{x - X_{M,i}} - \tan^{-1} \frac{y - Y_{A,i}}{x - X_{A,i}} \right). \tag{11}$$

In order to avoid singularities, we assume that each meron and antimeron is centered in the core of a plaquette, not on a lattice site. We show later that this condition can be relaxed. Then, the spin-distribution

$$S_x(\vec{r}) = (-1)^{(x+y)/a} S \cos \phi(\vec{r}) = S \,\mathrm{Re}\, e^{i[\phi(\vec{r})+\vec{Q}\cdot\vec{r}]}, \tag{12}$$

$$S_y(\vec{r}) = (-1)^{(x+y)/a} S \sin \phi(\vec{r}) = S \,\mathrm{Im}\, e^{i[\phi(\vec{r})+\vec{Q}\cdot\vec{r}]} \tag{13}$$

describes a locally AFM configuration, with has a 2π spin vortex around any center $R_{M,i}$ and a -2π spin-antivortex around any center $\vec{R}_{A,i}$. In Fig. 8, upper panel, we show a typical initial configuration obtained in this manner. While Eqs. (11)–(13) insure the appearance of the vortices around the chosen plaquettes, they do not enforce cyclic boundary conditions. For instance, the $y=1$, $x=2, \ldots, 5$ spins are parallel, not antiparallel, to the spins on the opposite boundary $y=20$, $x=2, \ldots, 5$, etc. Such ferromagnetically aligned regions act effectively as short stripes, and therefore may influence the magnetic structure factor considerably. In order to eliminate such unwanted contributions, we reinforce the cyclic boundary conditions through a simple iterative process. We first update the spins of one magnetic sublattice by aligning them antiparallel to the sum of their four nearest neighbor spins (in effect lowering the exchange energy). Then we update the spins on the second magnetic sublattice in the same way, until successive iterations no longer modify the spin distribution. However, we do not change the orientation of any of the four spins on the corners of any of the plaquettes on which a vortex or antivortex is centered. If we allow these spins to be updated in the same way, we see how from iteration to iteration merons get closer to antimerons and eventually annihilate each other, leading to a final long-range AFM state (corresponding to an absolute minimum total exchange energy). In the real system, meron-antimeron annihilation is prevented by the Coulomb repulsion between the charges trapped in their cores. We enforce this by not allowing the merons and antimerons to change their positions. The final configuration obtained for the initial snapshot shown in the upper panel of Fig. 8 is shown in the lower panel of Fig. 8. By comparison to the upper panel, it is apparent that only the spins near the boundaries have rearranged their orientations so that locally AFM ordering is reinforced.

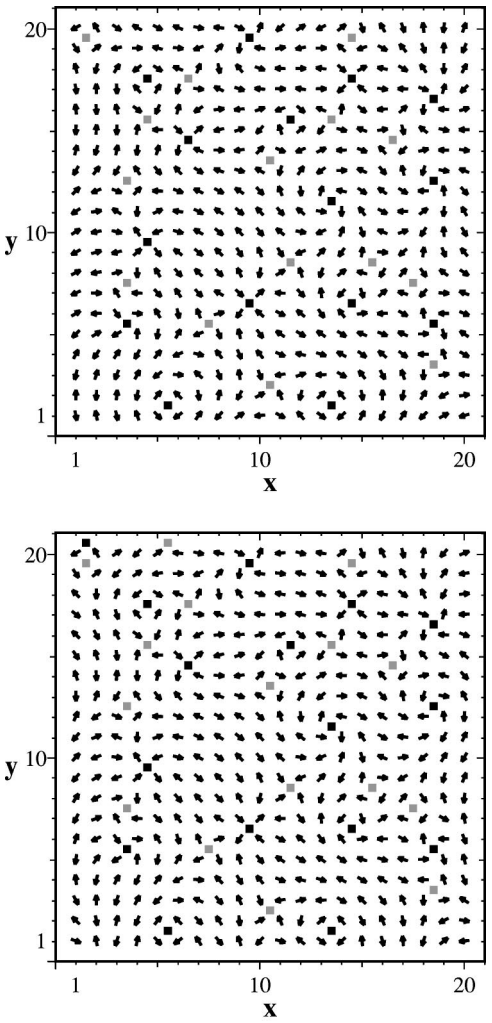

FIG. 8. Upper panel: spin distribution $\vec{S}(\vec{r})$ for a random collection of 15 merons and 15 antimerons on a 20×20 lattice. The merons are centered on plaquettes marked by dark squares, while the antimerons are centered on plaquettes marked by light squares. Lower panel: same distribution as in the upper panel, but with cyclic boundary conditions imposed. This leads to the appearance of an extra meron [centered at (1.5, 20.5)] and antimeron [centered at (5.5, 20.5)].

We note that our iterative procedure sometimes leads to the appearance of one or more new pairs of vortices near (or on) the boundary plaquettes. In Fig. 8, one new pair appears in the lower panel, with the vortex centered at (1.5, 20.5) and the antivortex centered at (5.5, 20.5). We cannot predict *a priori* precisely how many new pairs of vortices will be generated on the boundaries for any initial random distribution. However, the appearance of new vortices changes the effective "doping," $\delta = 2N_0/N^2$. To compensate for this, we start our simulations with a somewhat smaller number of vortices than that corresponding to the doping under consideration. We adjust this initial number of vortices such that the average doping is the desired one, once the cyclic boundary conditions have been imposed. We average for 1000 initial random configurations of merons and antimerons. Each final configuration (snapshot) thus generated is assigned an equal statistical weight in computing the average magnetic structure factor.

For an $N \times N$ lattice with cyclic boundary conditions, the linear resolution in the momentum space is $2\pi/Na$. In order to insure that this resolution is smaller than $2\delta\pi/a$ (the shift of the experimentally observed incommensurate peaks), we choose the linear dimension of the lattice $N \geqslant 1/\delta$. For all the simulations shown here, $N=100$ (we verified in a few cases that the average magnetic structure factor is unchanged for different N).

The resulting average structure factor for $0.02 \leqslant \delta < 0.05$ exhibits four incommensurate peaks diagonally aligned [see Figs. 9(a) and 9(b)]. In all cases there is considerable overlap of the four incommensurate peaks. This type of diagonal alignment is precisely what is observed experimentally for extremely underdoped samples. (For dopings $\delta < 0.02$ the four incommensurate peaks merge into the AFM Bragg peak, as already discussed).

Typical results obtained for runs with $\delta \geqslant 0.05$ are summarized in Figs. 10 and 11. In Fig. 10 we plot the ensemble averaged structure factor corresponding to doping $\delta = 0.100 \pm 0.003$. [The histogram of the number of final snapshots with number N_0 of vortex-antivortex pairs (on a 100×100 lattice) is shown in Fig. 11]. As expected, the nucleation of vortices leads to a suppression of the structure factor at the AFM wave-vector $Q = (\pi/a, \pi/a)$. Instead, four broad shifted peaks appear, with horizontal and vertical (collinear) displacements.

In Figs. 12 and 13 we plot the average magnetic structure factor corresponding to dopings $\delta = 0.05$, 0.10, and 0.15, along the various cuts in the Brillouin zone indicated in the insets. The positions of the experimentally measured peaks are also marked in all graphs, and they are found to be in excellent agreement with our results. The collinear shift of the incommensurate peaks can be found more precisely by fitting sums of Gaussians to these profiles. The results obtained for $\delta \geqslant 0.05$ are summarized in Fig. 14. The full circles show the results obtained for liquids of merons and antimerons, while empty circles and squares show the experimentally measured displacements for Sr and Nd-doped LaCuO samples.[5] For $\delta \leqslant 0.12$ the agreement is excellent. For $\delta > 0.12$, the experimentally measured shifts saturate, while the ones obtained from our simple model of the meron-antimeron liquid continue to increase linearly with doping. As we discuss later, this discrepancy is removed within a more accurate description which takes into consideration the effects of the second length scale, the vortex core size ρ.

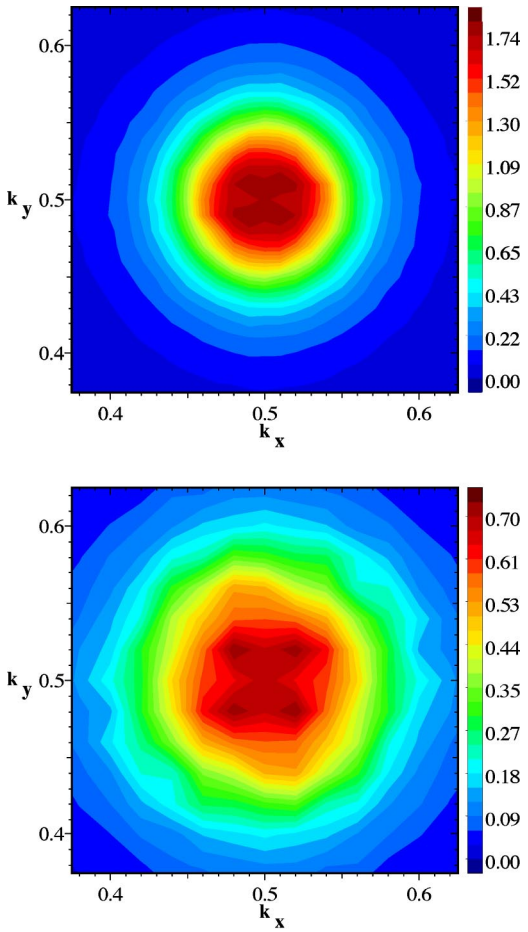

FIG. 9. The average structure factor for 1000 random configurations corresponding to the average dopings $\delta = 0.02$ (upper) and $\delta = 0.04$ (lower panel). The wave vectors are measured in units of $2\pi/a$. The four incommensurate peaks are aligned along the diagonals, in agreement with experimental observations for such extremely underdoped samples.

An explanation for the results summarized in Fig. 14 can be obtained if we analyze the contribution to the magnetic structure factor of meron-antimeron pairs. For $\delta > 0.02$ various meron-antimeron pairs overlap and we can regard the ground state as a liquid of meron-antimeron pairs which experience dissociations and recombinations as the vortices move around and interact with one another. The magnetic structure factor is, to first order, a sum of the contributions of individual meron-antimeron pairs, where for a given snapshot each meron is considered "paired" to its closest antimeron.

In Figs. 15(a) and 15(b) we show the magnetic structure factors for the single meron-antimeron pairs depicted in Figs. 16(a) and 16(b), respectively. We consider fairly large lattices to have a good resolution in the Brillouin zone. At the same time, we consider a meron-antimeron separation which is comparable to the lattice size. [If the pair is tightly bound (small) as in Fig. 7, the contribution of the pair is hidden by

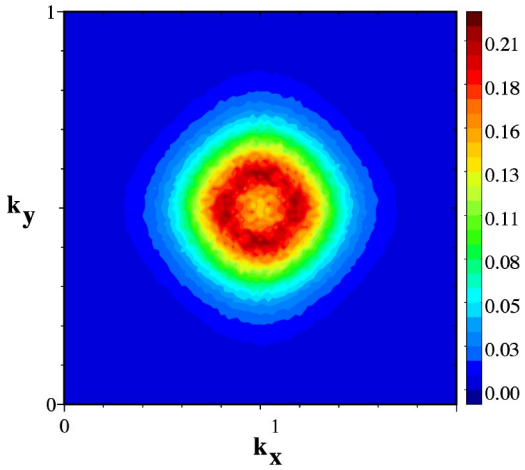

FIG. 10. The average structure factor of 1000 random configurations corresponding to an average doping $\delta=0.100\pm0.003$ (also, see Fig. 11). The wave vectors are measured in units of $2\pi/a$. The structure factor is suppressed at the AFM wave-vector $Q=(\pi/a,\pi/a)$ but exhibits four displaced peaks.

the dominant contribution of the background spins to the AFM peak at $\vec{Q}$]. As seen in Figs. 16(a) and 16(b), the line connecting the meron and the antimeron has the characteristics of an AFM domain wall (line defect). Crossing this line, along an orthogonal path, we observe a π flip in the AFM orientation of the spins. As discussed, such domain walls lead to the appearance of incommensurate peaks in the magnetic structure factor, whose displacement from the AFM peak is inversely proportional to the average (transverse) distance between domain walls. For the meron-antimeron pairs

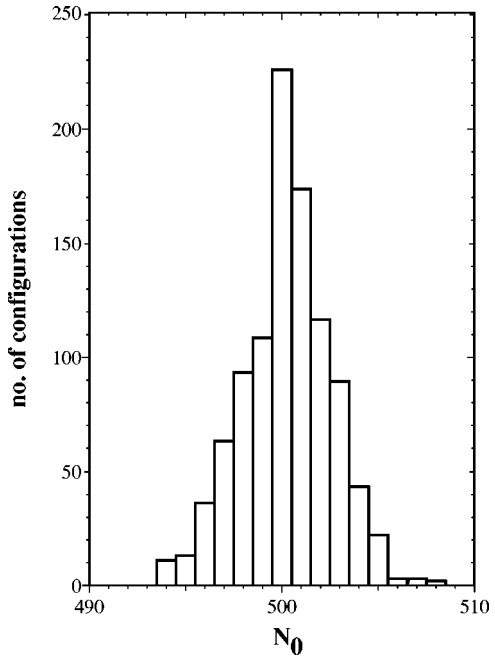

FIG. 11. Histogram showing the number of configurations corresponding to a given number N_0 of pairs of vortices and antivortices in the set of 1000 random configurations whose average structure factor is shown in Fig. 10.

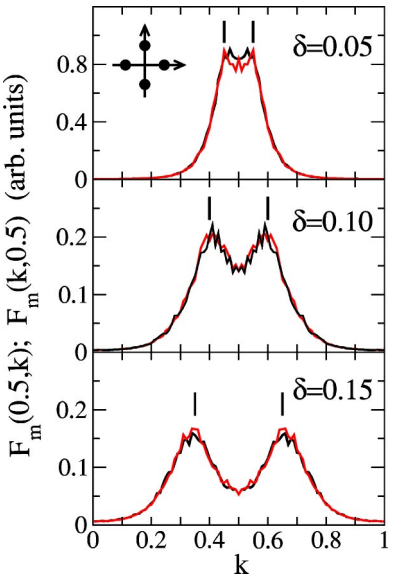

FIG. 12. Average magnetic structure factor along two directions in the Brillouin zone indicated in the inset, for dopings $\delta=0.05$, 0.10, 0.15. The wave vector is measured in units of $2\pi/a$. The positions of the experimentally measured peaks are indicated on each graph (short lines), and are found to be in excellent agreement with those predicted in our model.

shown in Figs. 16(a) and 16(b) (with periodic boundary conditions) this transverse separation is simply the size of the sample ($N=10$). Consequently, the peaks are shifted by $\pm0.1(2\pi/a)$ in Figs. 15(a) and 15(b), in a direction transversal to the meron-antimeron backbone.

Any snapshot of a liquid ground state has various pairs with various orientations and at various distances from each other. Each pair gives a maximum contribution to the magnetic structure factor for wave vectors shifted from $\vec{Q}$ in a direction perpendicular to the meron-antimeron backbone. The shift is of order $2\pi/d_t$, where d_t is the average transverse

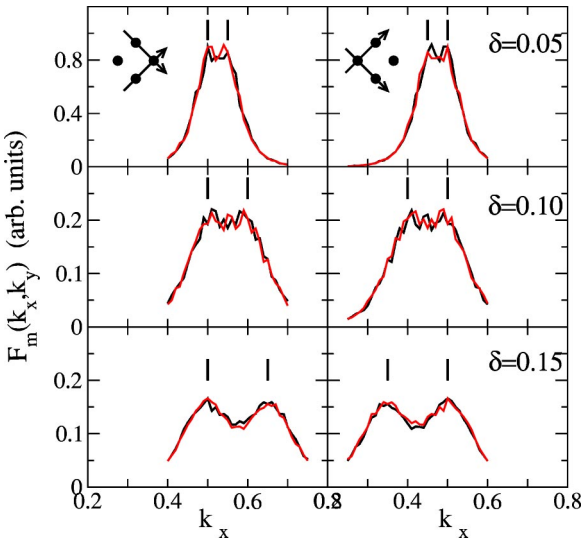

FIG. 13. Same as in Fig. 12, but for different cuts in the Brillouin zone, as indicated in the insets.

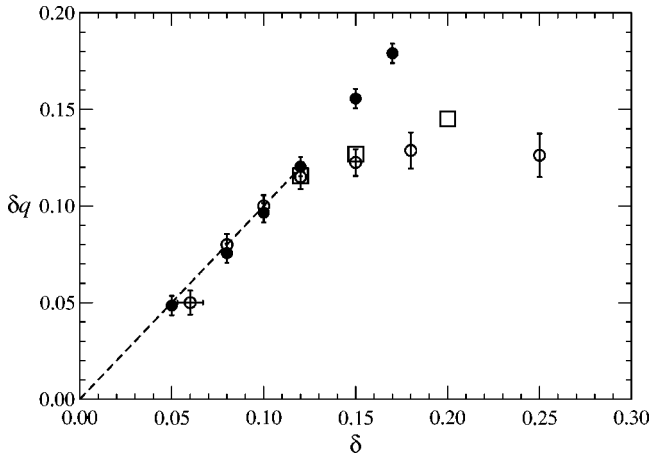

FIG. 14. The collinear shift δ_q, in units of $2\pi/a$, as a function of the doping δ. The full circles indicate the results obtained for liquids of merons and antimerons. The empty circles are experimental results for Sr-doped samples, and the squares are experimental results for Nd-doped samples, from Ref. 5.

separation between pairs. The average area occupied by a pair is $a^2/\delta = d_t d_l$, where d_l is the average longitudinal (meron-antimeron) distance. Since the pairs are defined in terms of nearest neighbors, $d_l < d_t$. In particular, if d_l is roughly constant, it follows that $d_t \sim \delta$ and therefore the shifts scale like $1/\delta$. This is precisely the type of behavior uncovered in the numerical simulations (see Fig. 14). In fact, from Fig. 10 we can see that the peaks are quite broad and that there is also significant weight in the average structure factor along the diagonal direction (also see middle panel in Fig. 13), meaning that for $\delta = 0.10$ there is still a considerable fraction of pairs diagonally aligned. As δ increases, most of the weight becomes localized in the horizontal peaks, with the diagonal contribution considerably suppressed, as seen in the lower panel of Fig. 13 for $\delta = 0.15$. This is related to the fact that at higher dopings the increased number of pairs must be more closely packed, and therefore collinear arrangement is preferred. By symmetry, one expects roughly equal numbers of pairs with both the horizontal and vertical alignment, leading to the appearance of the four incommensurate peaks. On the other hand, for $\delta < 0.05$ the peaks are seen along the diagonals, implying that at such extremely low dopings pairs are mostly diagonally aligned, thus taking advantage of the increased area available to each pair.

The discrepancy between our simple model and experimental results for $\delta > 0.12$ can also be explained. The linearity of the shift with the doping obtained in our simulations of liquids of merons and antimerons, is simply a consequence of incorporating only one length scale, namely the (doping-controlled) average transverse distance between pairs of vortices. However, there is a second length scale in the system, given by the localization length of the hole in the vortex core. The trapping of the hole in the vortex core leads to a suppression of the magnitude of the spins in the vortex core, and this, in turn, affects the magnetic structure factor. In order to model this suppression, we should, in fact, use the spin distributions [see Eqs. (12) and (13)]

$$S_x(\vec{r}) \to S_x(\vec{r}) f(\vec{r}), \tag{14}$$

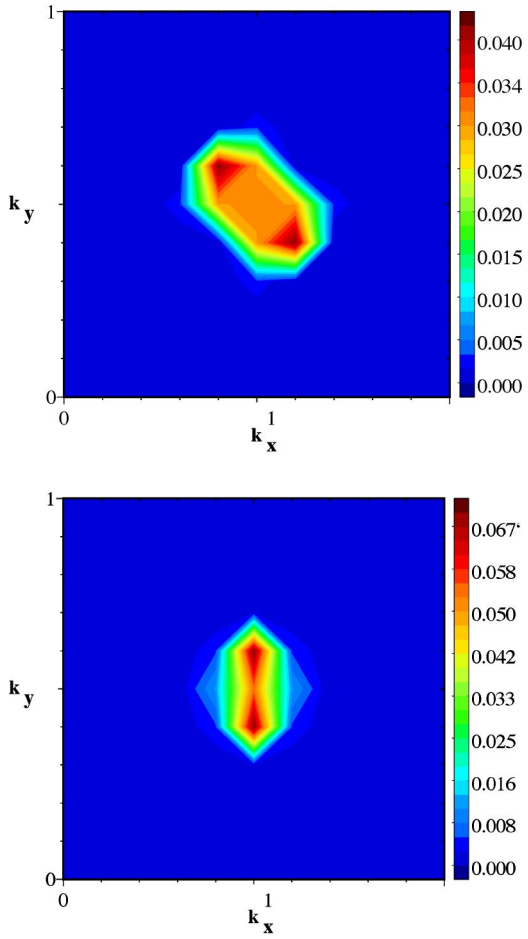

FIG. 15. The structure factors for the two meron-antimeron pairs shown in Figs. 16(a) and 16(b), respectively. The wave vector is measured in units of $2\pi/a$. In both cases, a pair of satellite peaks appears, with an orientation perpendicular to that of the meron-antimeron axis in real space.

$$S_y(\vec{r}) \to S_y(\vec{r}) f(\vec{r}) \tag{15}$$

with

$$f(\vec{r}) = \prod_{i=1}^{N_0} \tanh\left(\frac{|\vec{r} - \vec{R}_{M,i}|}{\rho}\right) \tanh\left(\frac{|\vec{r} - \vec{R}_{A,i}|}{\rho}\right), \tag{16}$$

where $\vec{R}_{A,i}$, $\vec{R}_{M,i}$, $i = 1, \ldots, N_0$ are the positions of the meron and antimeron cores, and ρ is the characteristic size of the vortex core, determined by the localization length of the hole inside the core. The introduction of the function $f(\vec{r})$ removes the necessity of asking that vortices are always centered on a plaquette. The case studied so far [see Eqs. (12) and (13)] corresponds to $\rho \to 0$. One expects this to be an acceptable approximation in the small doping regime, where the average distance between vortices is much larger than ρ. At higher dopings, however, the two length scales become comparable and the limit $\rho \to 0$ is no longer appropriate.

We computed the average structure factor for liquids of merons and antimerons corresponding to various dopings $\delta \geqslant 0.05$ and various core sizes ρ. In all cases, we observe the appearance of the four collinear incommensurate peaks, but

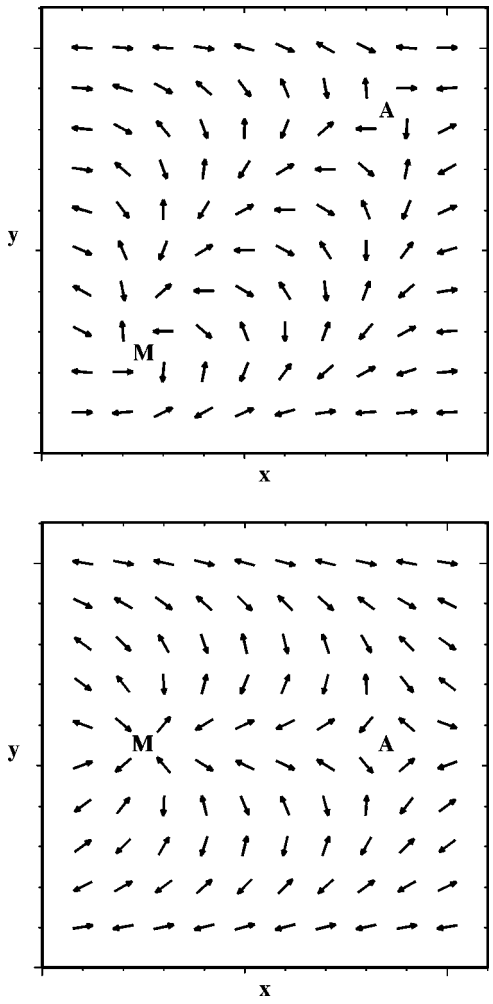

FIG. 16. A diagonal (top) and a horizontal (bottom) meron-antimeron pair is depicted. The corresponding magnetic structure factors are shown in Figs. 16(a) and 16(b).

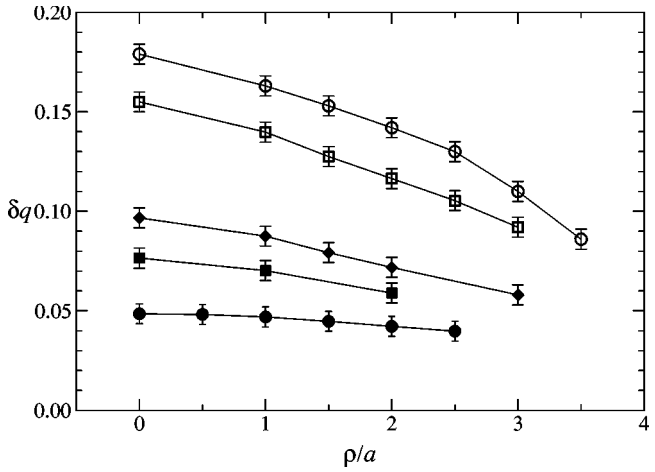

FIG. 17. The collinear shift δq, in units of $2\pi/a$, as a function of core size ρ (measured in lattice constant units a). The full circles, full squares, full diamonds, empty squares and empty circles correspond to $\delta=0.05$, 0.08, 0.10, 0.15, and 0.17, respectively. While for $\rho\to 0$ we have $\delta q\approx\delta$, for increasing ρ the shift δq decreases, and the effect is more pronounced for larger concentrations.

now their position depends both on δ and on ρ, as shown in Fig. 17. As expected, for small dopings there is little dependence of δq on ρ, with the shift δq being almost constant for $\delta=0.05$. However, for larger dopings ρ becomes important, and can lead to a significant decrease in the magnitude of the shift.

Since the core size ρ characterizes the localization of the hole in the vortex core, one must go beyond classical models in order to estimate it. Using the Hartree-Fock approximation described in Ref. 19, we can obtain the self-consistent spin configuration of an isolated vortex (see Fig. 1). The core size $\rho\sim t/US$,[25,26] where U characterizes the on-site repulsion, t is the hopping matrix and S is the magnitude of the staggered spin in the AFM undoped background. For $U/t=5$ we find $\rho/a=1.05\pm0.05$. The value $\rho/a=1$ (or smaller, for larger U/t values) can only be used for low concentrations, where the average inter-vortex distance is large enough that each vortex core can be treated as being isolated. As the doping increases and the vortex cores themselves start to overlap, the core radius ρ increases. This can also be seen from the fact that with increased doping the effective Mott-Hubbard gap $\Delta=US$ decreases both due to a decrease of the effective average spin S through suppression in the vortex cores, and also because of the direct filling of the Mott-Hubbard gap with localized levels on which the doping holes are trapped.[19,20] In fact, the Hartree-Fock calculations of Ref. 19 suggest that for $\delta\sim 0.30$ the Mott-Hubbard gap is completely closed and the ground state evolves towards a homogeneous Fermi-liquid metal, with a partially filled conduction band. This suggests that $\rho\to\infty$ for $\delta\sim 0.30$.

Comparing Figs. 14 and 17 we see that we get both the linear increase with δ for $\delta<0.12$, and the saturation above $\delta>0.12$ provided that $\rho/a\sim 1$ (or smaller) for $\delta<0.12$, and $\rho/a\sim 1.6$ and 2.6 for $\delta=0.15$ and 0.17, respectively. This fairly steep increase in ρ with δ needed to saturate the value of δq for $\delta>0.12$ is not unreasonable, if ρ is diverging as $\delta\to 0.30$. In fact, the existence of a limiting concentration δ for which ρ diverges is apparent in our simple model of the vortex distributions [Eqs. (12) and (13)]. For concentrations $\delta\geqslant 0.20$, we could not generate vortex configurations on the lattice. This happens because the four spins in the corners of each plaquette (on which a vortex or antivortex is centered) must satisfy the $\pm 2\pi$ vortex condition. This leads to frustration if too many vortices are being squeezed too close to one another. For $\delta\geqslant 0.20$, creation of new vortices with doping becomes impossible and a transition towards a homogeneous ground state must take place, i.e., $\rho\to\infty$.

IV. STRIPE PHASES OF THE MERON-VORTEX MODEL: SUPPRESSION OF SUPERCONDUCTIVITY AT 1/8 DOPING

The $\delta=1/8$ doping is very special, because in some compounds[34] superconductivity is suppressed at this doping. In a recent paper,[19] we demonstrated (using a static Hartree-Fock approximation and a very small anisotropy in the electron hopping) the appearance of a self-consistent ordered configuration of merons and antimerons at this doping. The

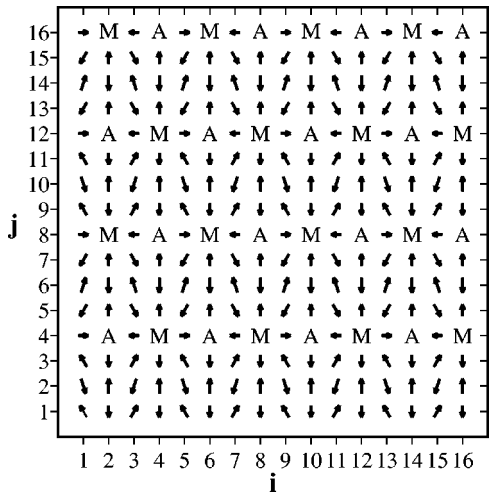

FIG. 18. Self-consistent spin distribution for the configuration of lowest energy found after adding a 3% anisotropy in the hopping integrals, at $\delta=1/8$, for $U/t=5$ in the spin-flux phase (from Ref. 19). The merons and antimerons arrange on horizontal lines, leading to a structure similar to that suggested by Tranquada in Ref. 28.

spin distribution of this configuration is shown in Fig. 18. This structure is very similar to the one proposed by Tranquada to explain the results obtained through neutron diffraction for charge and spin ordering in $La_{1.48}Nd_{0.4}Sr_{0.12}CuO_4$.[35] The Tranquada structure is schematically shown in Fig. 19. It consists of horizontal charged stripes, with holes localized every second site along the stripe backbone. The stripes are separated by AFM regions, with orientations π flipped across each stripe. The ordered crystal of merons and antimerons shown in Fig. 18 also has holes localized every second site along the backbone. In particular, there is a hole localized in the core of each meron and antimeron. Also, the regions between the backbones have (slightly distorted) AFM orientations, with the same π flip from one region to the next.

In our model charged merons and antimerons carry currents (and supercurrents). They are usually in a liquid-like ground state which allows for free motion along the planes. However, for $\delta=1/8$ we see that this liquid crystallizes to an ordered ground state in which the charge carriers are frozen. This offers a very simple and natural explanation for the suppression of superconductivity at this particular doping. This crystallization of the merons and antimerons is induced by Nd doping, which leads to an experimentally observed distortion of the lattice from the usual low-temperature orthorhombic (LTO) structure to the low-temperature tetragonal (LTT) structure at $1/8$ doping.[35] In the LTT phase the atomic structural displacements align along horizontal (or vertical) directions, and very likely favor the pinning of the merons and antimerons along horizontal (vertical) "stripes," thus suppressing superconductivity.

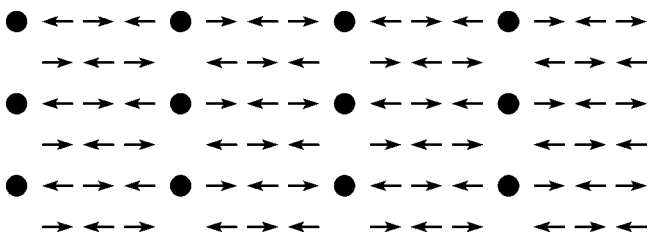

FIG. 19. Stripe configuration suggested by Tranquada in Ref. 28, in order to explain results obtained through neutron diffraction for charge and spin ordering in $La_{1.48}Nd_{0.4}Sr_{0.12}CuO_4$.

V. CONCLUSIONS

We have investigated, in detail, the magnetic structure factor of liquids of merons and antimerons in a doped 2D spin-1/2 antiferromagnet, using a simple model. The only parameters in this model are the doping concentration δ, which determines the number of merons and antimerons, and the core size ρ describing the localization of the hole inside the vortex core.

At low and intermediate dopings $\delta \leqslant 0.12$, where $\rho \ll 1/\delta$, we obtain excellent quantitative agreement with the experimental measurements. We observe both the linear dependence of the shift of the incommensurate peaks on the doping δ, as well as the rotation of the position of the peaks from diagonal alignment (below $\delta=0.05$) to collinear alignment (above $\delta=0.05$). For larger dopings, a nontrivial core size ρ is required to account for the saturation of the magnetic peak shift with δ (see Fig. 17) for $\delta > 0.12$. While we argued that such a dependence is reasonable, a detailed investigation of the dependence of ρ on δ and other microscopic parameters must be performed to confirm this picture.

In obtaining these results, we averaged uniformly over random vortex configurations. In other words, we did not use any selection criterion for "preferred" configurations. However, a more detailed theory may require a more sophisticated choice for the vortex pair distribution functions. Recently[6] it was reported that LaSrCuO crystals doped at $\delta=0.04$ and 0.05 exhibit only one of the two pairs of diagonal incommensurate peaks, not both of them. It is also known that these crystals are in a low-temperature orthorombic phase (LTO), in which the CuO_6 octahedra coherently tilt along the [110] direction (or $[1\bar{1}0]$, leading to twinning). Due to this tilt, the two diagonal directions are no longer equivalent, favoring alignment of the meron-antimeron pairs along the shorter diagonal. In turn, this will lead to higher weight in one of the pairs of incommensurate peaks. Another recent experimental observation[7] is that in LaSrCuO and $LaCuO_{4+\delta}$ samples (with doping $\delta=0.12$) the four incommensurate peaks are not truly collinear, but at an angle of about 3° with the horizontal and vertical directions. This also suggests an underlying distortion which favors slightly tilted meron-antimeron pairs. Such considerations are similar to the one discussed in Sec. IV, where we argued that Nd-induced structural distortions lead to the pinning of the merons and antimerons into the Tranquada configurations.

It is very interesting to note that the magnetic signatures we describe are most clearly seen in the LaCuO. This compound has an anomalously low superconducting temperature T_c and its CuO planes support various types of tilting, depending on temperature, doping, nature of dopants, etc. All these distortions are responsible for pinning and/or slowdown of the dynamics of merons and antimerons. Such pinning or slowdown of these charge carriers offers a possible

explanation for the suppression of superconductivity. This is most obvious for the $\delta = 1/8$ case, where merons and antimerons assemble into static stripe-like configurations. This also provides an answer to the long-standing question of why stripes seem to compete with superconductivity and, more generally, why charge carrier dynamics correlates with a high superconducting temperature.

In conclusion, our model of a liquid of charged meron-antimeron pairs quantitatively explains the orientation and position (as a function of doping) of the four incommensurate magnetic peaks observed through elastic neutron scattering. In previous work[19,20] we have shown that this same microscopic model provides a unified basis for non-Fermi-liquid transport properties, *d*-wave preformed charged carrier pairs, midinfrared optical absorption, and certain aspects of ARPES. We therefore believe that this microscopic model for cuprate high-temperature superconductors is worthy of more detailed investigation and comparison with experiment.

ACKNOWLEDGMENTS

We are grateful to Dr. Gabe Aeppli for a stimulating discussion. This work was supported in part by the Natural Sciences and Engineering Research Council of Canada.

[1] S. W. Lovesey, *Theory of Neutron Scattering from Condensed Matter* (Clarendon Press, Oxford, 1984), Vol. 2.

[2] D. Vaknin, S. K. Sinha, D. E. Moncton, D. C. Johnston, J. M. Newsam, C. R. Safinya, and H. E. King Jr., Phys. Rev. Lett. **58**, 2802 (1987).

[3] D. J. M. Tranquada *et al.*, Phys. Rev. Lett. **60**, 159 (1988).

[4] See, for instance, D. M. Ginsberg, *Physical Properties of High Temperature Superconductors* (World Scientific, Singapore 1992), Vol. I-V.

[5] K. Yamada, C. H. Lee, K. Kurahashi, J. Wada, S. Wakimoto, S. Ueki, H. Kimura, Y. Endoh, S. Hosoya, G. Shirane, R. J. Birgeneau, M. Greven, M. A. Kastner, and Y. J. Kim, Phys. Rev. B **57**, 6165 (1998), and references therein.

[6] S. Wakimoto, R. J. Birgeneau, M. A. Kastner, Y. S. Lee, R. Erwin, P. M. Gehring, S. H. Lee, M. Fujita, K. Yamada, Y. Endoh, K. Hirota, and G. Shirane, Phys. Rev. B **61**, 3699 (2000).

[7] H. Kimura, H. Matsushita, K. Hirota, Y. Endoh, K. Yamada, G. Shirane, Y. S. Lee, M. A. Kastner, and R. J. Birgeneau, Phys. Rev. B **61**, 14366 (2000); H. Kimura, K. Hirota, H. Matsushita, K. Yamada, Y. Endoh, S.-H. Lee, C. F. Majkrzak, R. Erwin, G. Shirane, M. Greven, Y. S. Lee, M. A. Kastner, and R. J. Birgeneau, *ibid.* **59**, 6517 (1999); Y. S. Lee, R. J. Birgeneau, M. A. Kastner, Y. Endoh, S. Wakimoto, K. Yamada, R. W. Erwin, S.-H. Lee, and G. Shirane, *ibid.* **60**, 3643 (1999).

[8] P. Dai, H. A. Mook, R. D. Hunt, and F. Dogan, Phys. Rev. B **63**, 054525 (2001); M. Arai, T. Nishijima, Y. Endoh, T. Egami, S. Tajima, K. Tomimoto, Y. Shiohara, M. Takahashi, A. Garrett, and S. M. Bennington, Phys. Rev. Lett. **83**, 608 (1999); H. F. Fong, P. Bourges, Y. Sidis, L. P. Ragnault, J. Bossy, A. Ivanov, D. L. Milius, I. A. Aksay, and B. Keimer, Phys. Rev. B **61**, 14773 (2000).

[9] H. A. Mook, P. Dai, S. M. Hayden, G. Aeppli, T. G. Perrings, and F. Dogan, Nature (London) **395**, 580 (1998).

[10] P. B. Littlewood, J. Zaanen, G. Aeppli, and H. Monien, Phys. Rev. B **48**, 487 (1993); Q. Si, Y. Zha, K. Levin, and J. P. Lu, Phys. Rev. B **47**, 9055 (1993); P. Benard, L. Chen, and A.-M. S. Tremblay, *ibid.* **47**, 15217 (1993).

[11] B. O. Wells, Z.-X. Shen, A. Matsuura, D. M. King, M. A. Kastner, M. Greven, and R. J. Birgeneau, Phys. Rev. Lett. **74**, 964 (1995); S. LaRosa, I. Vobornik, F. Zwick, H. Berger, M. Grioni, G. Margaritondo, R. J. Kelley, M. Onellion, and A. Chubukov, Phys. Rev. B **56**, R525 (1997); F. Ronning, C. Kim, K. M. Shen, N. P. Armitage, A. Damascelli, D. H. Lu, D. L. Feng, Z.-X. Shen, L. L. Miller, Y.-J. Kim, F. Chou, and I. Terasaki, *ibid.* **67**, 035113 (2003).

[12] C. Kim, P. J. White, Z.-X. Chen, T. Tohyama, Y. Shibata, S. Maekawa, B. O. Wells, Y. J. Kim, R. J. Birgeneau, and M. A. Karstner, Phys. Rev. Lett. **80**, 4245 (1998).

[13] D. S. Marshall, D. S. Dessau, A. G. Loesser, C.-H. Park, A. Y. Matssura, J. N. Eckstein, I. Bozovic, P. Fournier, A. Kapitulnik, W. E. Spicer, and Z.-X. Shen, Phys. Rev. Lett. **76**, 4841 (1996).

[14] S. John and P. Voruganti, Phys. Rev. B **43**, 10815 (1991); S. John, P. Voruganti, and W. Goff, Phys. Rev. B **43**, 13365 (1991); P. Voruganti, A. Golubentsev, and S. John, *ibid.* **45**, 13945 (1992).

[15] D. Poilblanc and T. M. Rice, Phys. Rev. B **39**, 9749 (1989); H. J. Schultz, J. Phys. (Paris) **50**, 2833 (1989).

[16] M. Kato, K. Machida, H. Nakanishi, and M. Fujita, J. Phys. Soc. Jpn. **59**, 1047 (1990); K. Machida, Physica C **158**, 192 (1989).

[17] J. Zaanen and O. Gunnarson, Phys. Rev. B **40**, 7391 (1989); J. Zaanen, M. L. Horbach, and W. van Saarloos, *ibid.* **53**, 8671 (1996).

[18] I. F. Herbut and D. J. Lee, Phys. Rev. B **68**, 104518 (2003).

[19] M. Berciu and S. John, Phys. Rev. B **59**, 15143 (1999).

[20] M. Berciu and S. John, Phys. Rev. B **61**, 16454 (2000).

[21] M. Berciu and S. John, Physica B **296**, 143 (2001).

[22] T. Tohyama, C. Gazza, C. T. Shih, Y. C. Chen, T. K. Lee, S. Maekawa, and E. Dagotto, Phys. Rev. B **59**, R11649 (1999); S. R. White and D. J. Scalapino, *ibid.* **60**, R753 (1999); B. Valenzuela, M. A. H. Vozmediano, and F. Guinea, *ibid.* **62**, 11312 (2000); B. Normand and A. P. Kampf, *ibid.* **65**, 020509 (2002).

[23] S. John and A. Golubentsev, Phys. Rev. Lett. **71**, 3343 (1993).

[24] S. John and A. Golubentsev, Phys. Rev. B **51**, 381 (1995).

[25] S. John, M. Berciu, and A. Golubentsev, Europhys. Lett. **41**, 31 (1998).

[26] M. Berciu and S. John, Phys. Rev. B **57**, 9521 (1998).

[27] M. Berciu and S. John, Phys. Rev. B **61**, 10015 (2000).

[28] J. M. Tranquada, B. J. Sternlieb, J. D. Axe, Y. Nakamura, and S. Uchida, Nature (London) **375**, 561 (1995); J. M. Tranquada, J. D. Axe, N. Ichikawa, Y. Nakamura, S. Uchida, and B. Nachumi, Phys. Rev. B **54**, 7489 (1996).

[29] G. Xu, G. Aeppli, M. E. Bisher, C. Broholm, J. F. DiTusa, C. D. Frost, T. Ito, K. Oka, R. L. Paul, H. Takagi, and M. M. J. Treacy, Science **289**, 419 (2000).

[30] S. R. White and D. J. Scalapino, Phys. Rev. Lett. **81**, 3227 (1998).

[31] M. Fleck, A. I. Lichtenstein, E. Pavarini, and A. M. Oles, Phys.

Rev. Lett. **84**, 4962 (2000).

[32] C. S. Hellberg and E. Manousakis, Phys. Rev. Lett. **83**, 132 (1999); S. R. White and D. J. Scalapino, Phys. Rev. Lett. **84**, 3021 (2000); C. S. Hellberg and E. Manousakis, *ibid.* **84**, 3022 (2000).

[33] V. J. Emery and S. A. Kivelson, Physica C **209**, 597 (1993); **235–240** , 189 (1994); in *Proceedings of the Los Alamos Symposiun on Strongly Correlated Electronic Materials, 1993*, edited by K. S. Bedell (Addison-Wesley, Reading, MA, 1994).

[34] A. R. Moodenbaugh, Y. Xu, M. Suenaga, T. J. Folkerts, and R. N. Shelzen, Phys. Rev. B **38**, 4596 (1988).

[35] M. K. Crawford, R. L. Harlow, E. M. McCarron, W. E. Farneth, J. D. Axe, H. Chou, and Q. Huang, Phys. Rev. B **44**, 7749 (1991); J. D. Axe, A. H. Moudden, D. Hohlwein, D. E. Cox, K. M. Mohanty, A. R. Moodenbaugh, and Youwen Xu, Phys. Rev. Lett. **62**, 2751 (1989); B. Buchner, M. Breuer, A. Freimuth, and A. P. Kampf, J. Low Temp. Phys. **95**, 285 (1994).